THE RELATIONSHIPS BETWEEN KAOLINITE CRYSTAL PROPERTIES AND THE ORIGIN OF MATERIALS FOR A BRAZILIAN KAOLIN DEPOSIT

ANGÉLICA F. DRUMMOND C. VARAJÃO,[1] ROBERT J. GILKES,[2] AND ROBERT D. HART[2]

[1] DEGEO/EM/UFOP, Campus Morro do Cruzeiro, 35400-000 Ouro Preto, MG, Brazil
[2] Soil Science and Plant Nutrition, Faculty of Agriculture, The University of Western Australia, Nedlands, Western Australia 6907, Australia

Abstract—The clay particles in a kaolin deposit from Brazil were investigated by X-ray diffraction (XRD), differential thermal analysis (DTA), analytical transmission electron microscopy (ATEM), and electron paramagnetic resonance (EPR) to examine the relationships between morphological and chemical properties of the crystals and to relate these properties to formation conditions. The XRD patterns show the dominant presence of kaolinite with minor amounts of gibbsite, illite, quartz, goethite, hematite, and anatase. ATEM observations show two discontinuities in the deposit as indicated by changes in morphology and size of the kaolinite crystals. At the base of the deposit, hexagonal platy and lath-shaped particles (mean area of 001 face = 0.26 μm^2) maintain the original fabric of the parent rock which characterizes an *in situ* evolution. In the middle of the deposit a bimodal population of large (mean area of 001 face > 0.05 μm^2) and small (mean area of 001 face < 0.05 μm^2) sub-hexagonal platy kaolinite crystals occurs. This zone defines the boundary between the saprolitic kaolinite and the pedogenic kaolinite. Near the top of the profile, laths and irregular plates of kaolinite, together with sub-hexagonal particles, define two different depositional sources in the history of formation of the deposit. Crystal thickness as derived from the width of basal reflections and the Hinckley index are compatible with the morphological results, but show only one discontinuity. At the base of the deposit, kaolinite has a low-defect density whereas in the middle and at the top of the profile, kaolinite has a high-defect density. Likewise, EPR spectroscopy shows typical spectra of low-defect kaolinite for the bottom of the deposit and typical spectra of high-defect kaolinite for the other portions of the deposit. Despite the morphological changes observed through the profile, the elemental composition of individual kaolinite crystals did not show systematic variations. These results are consistent with the deposit consisting of a transported pedogenic kaolinite over saprolite consisting of *in situ* kaolinized phyllite.

Key Words—ATEM, Defect, EPR, Formation Condition, Kaolinite, Morphology, Saprolite, Soil, XRD.

INTRODUCTION

Kaolinite is an important weathering product at low latitudes. It is a common constituent of saprolites and the most abundant clay mineral in the overlying soils (Dixon, 1989). Kaolinite can be formed by *in situ* chemical evolution (weathering) of the underlying rocks and from colluvial materials derived from highly weathered lateritic profiles (Gilkes *et al.*, 1973; Mulcahy, 1973). According to the AIPEA Nomenclature Committee Report (Guggenheim *et al.*, 1997), the term kaolin may be either a mineral group name or a rock name. In the present work, kaolinite is designated as a mineral name and kaolin is used only as a rock name.

Crystals of kaolinite in saprolite and in kaolin deposits are typically large (1–2 μm) hexagonal plates (Dixon, 1989), although various shapes (Keller, 1978), such as laths and pseudo-hexagonal plates, may occur. In marked contrast, kaolinite in topsoil horizons commonly consists of small anhedral platy to tubular particles (Singh and Gilkes, 1992a). Such variability in kaolinite morphology is common and widespread in natural deposits. Similarly, the defect density and probably chemical composition of kaolinite may differ among occurrences and this may influence the surface chemical and physical properties of clay materials (Robson and Gilkes, 1981; McCrea *et al.*, 1990).

Many studies relating the defect densities in kaolinite to chemical composition have been performed since the early work of Robertson *et al.* (1954), and several techniques using spectroscopic methods were proposed to investigate defect concentrations (Jones *et al.*, 1974; Angel *et al.*, 1974; Meads and Malden, 1975; Herbillon *et al.*, 1976; Mestdagh *et al.*, 1980; Brindley *et al.*, 1986). These studies showed that both the content and the location of structural iron may involve relationships with the defect densities in kaolinites, although the mechanisms responsible for these relationships are unknown. There is some understanding of the geochemical process that controls the composition of kaolinite formed during weathering (Muller *et al.*, 1995), but the great variability in iron content and morphology of kaolinite in soils (Singh and Gilkes, 1995; Hart *et al.*, unpubl. data) raises questions about the role of the iron content of kaolinite in affecting crystal properties. For example, does iron in solution or as crystalline phases during the formation of kaolinite affect crystal growth or is iron accidentally incorporated into the kaolinite so that the extent of incorporation is affected by crystal morphology and not the reverse (Stone and Torres-Sanchez, 1988).

The present study focuses on the morphological and chemical features of kaolinite crystals from Brazil and the relationship to formation conditions in a low-temperature environment. The deposit, sampled from a drill core, was formed by the superposition of a colluvial unit upon an *in situ* saprolitic unit (Varajão *et al.,* 1989, 1990, 2000). This study allows us to distinguish the processes of formation of the kaolinite and is potentially useful for mineral exploration in highly weathered terrains and for interpreting geological history.

Size and morphology of the kaolinite crystals were examined by high-resolution transmission electron microscopy (HRTEM), and the elemental composition of single crystals was obtained by energy dispersive spectroscopy (EDS). Bulk chemical analyses, X-ray diffraction (XRD) patterns, and electron paramagnetic resonance spectroscopy (EPR) were used to determine the defect content and crystal chemistry of kaolinite.

LOCATION AND GEOLOGICAL SETTING

The study is based on samples from a kaolin deposit located 15.5 km from Belo Horizonte, capital of the Minas Gerais State, southeastern Brazil (Figure 1). The kaolin deposit is situated in the Moeda Syncline trough on the western border of the Quadrilátero Ferrífero, a mountainous Precambrian region with altitudes varying from 650 to 2000 m and with an area of ~7000 km². The main geomorphologic features of this syncline are related to both lithologic and structural control. The syncline is characterized by crest lines consisting of itabirite and quartzite rocks bordering depressions originating from differential weathering of the substratum consisting of sericitic schists, phyllitic dolomite, and dolomitic itabirite. Many economically important kaolin deposits occur in these depressions and one is characterized here.

Owing to their economic interest and because these deposits belong to a well-known structural unit of the Quadrilátero Ferrífero, their origin has been studied by field observations and relatively unsophisticated mineralogical analysis. Thus, according to Pomerene (1964) and Souza (1983), these deposits result from an *in situ* evolution from alluvial sediments within karstic depressions (Dorr, 1969; Fleisher and Oliveira, 1969; Barbosa, 1980). Souza (1983) suggested that sediments were derived from carbonatic phyllite and Fleisher and Oliveira (1969) suggested that they originated from basic rocks. In both hypothesis, these sediments were subjected to climatic and hydrological variations. More recent studies (Varajão *et al.,* 1989, 1990, 2000) based on petrological analysis revealed a more complex genesis for these occurrences involving the superposition of two units. The lower unit shows an *in situ* evolution from the underlying phyllitic rocks. The upper unit is allochtonous and was derived from lateritic (Miocene age) colluvial material origi-

nating from the weathering of phyllitic rocks that comprised the adjoining slopes.

MATERIALS AND METHODS

Six samples, from depths of 76, 58, 54, 24, 13, and 10 m, representing the general evolution of the profile, were selected from a core drilled through the entire clayey sequence and the saprolite (Figure 1). Extractable Fe, Al, and Si were dissolved using, successively, three extractants: sodium pyrophosphate (Blakemore *et al.,* 1981), acid ammonium oxalate (Tamm, 1922; McKeague and Day, 1966), and citrate-dithionite (Holmgren, 1967). Content was determined with a Perkin-Elmer Analyst 300 atomic absorption spectrophotometer. The XRD patterns of whole samples and the clay fraction, as both oriented and random samples, were obtained before and after the extractions with a Philips PW 3020 diffractometer, using monochromatic CuKα radiation. The full-width at half-maximum (FWHM) of the XRD peak and the size of coherently scattering domains (CSD) of crystals, as calculated from the FWHM and the Scherrer equation (Klug and Alexander, 1974), were determined from samples of (001) oriented clay-mineral aggregates. Hinckley (Hinckley, 1963) and HB (Hughes and Brown, 1979) indexes were measured from the XRD patterns of samples of randomly oriented clay fractions. Differential thermal analysis (DTA) was performed on each sample using an SDT 2960 TA DTA-GTA instrument.

Chemical composition of the clay fraction after chemical extraction and Ca^{2+} saturation was obtained by X-ray fluorescence (XRF) analysis. Cation-exchange capacity (CEC) was determined by calculation from the chemical composition.

For analytical transmission electron microscopy (ATEM), specimens were prepared by two methods, dispersed samples and microtome sections. For the first, a highly diluted suspension of the <2-μm size fraction, after the sequential extraction described above, was prepared in distilled water and clay particles were dispersed by ultrasonic treatment. A drop of the suspension was deposited on a carbon-coated grid and dried at room temperature.

For ultramicrotomy, the clay fraction (<2 μm), after the sequential chemical extraction, was settled in a flat-bottomed plastic vessel and dried at 40°C. The dried samples were vacuum impregnated with Spurr's resin (Spurr, 1969) and thin sections, perpendicular to the (001) planes of the crystals, were cut with a diamond knife using a Reichert-Jung microtome.

Both dispersed samples and microtomed sections were studied using a Philips EM 430 electron microscope, which was equipped with an X-ray energy dispersive system, and operated at 300 kV. The ultrathin sections allowed us to measure the thickness of the kaolinite crystals and obtain lattice images of the basal spacing. To characterize the size and shape of the crys-
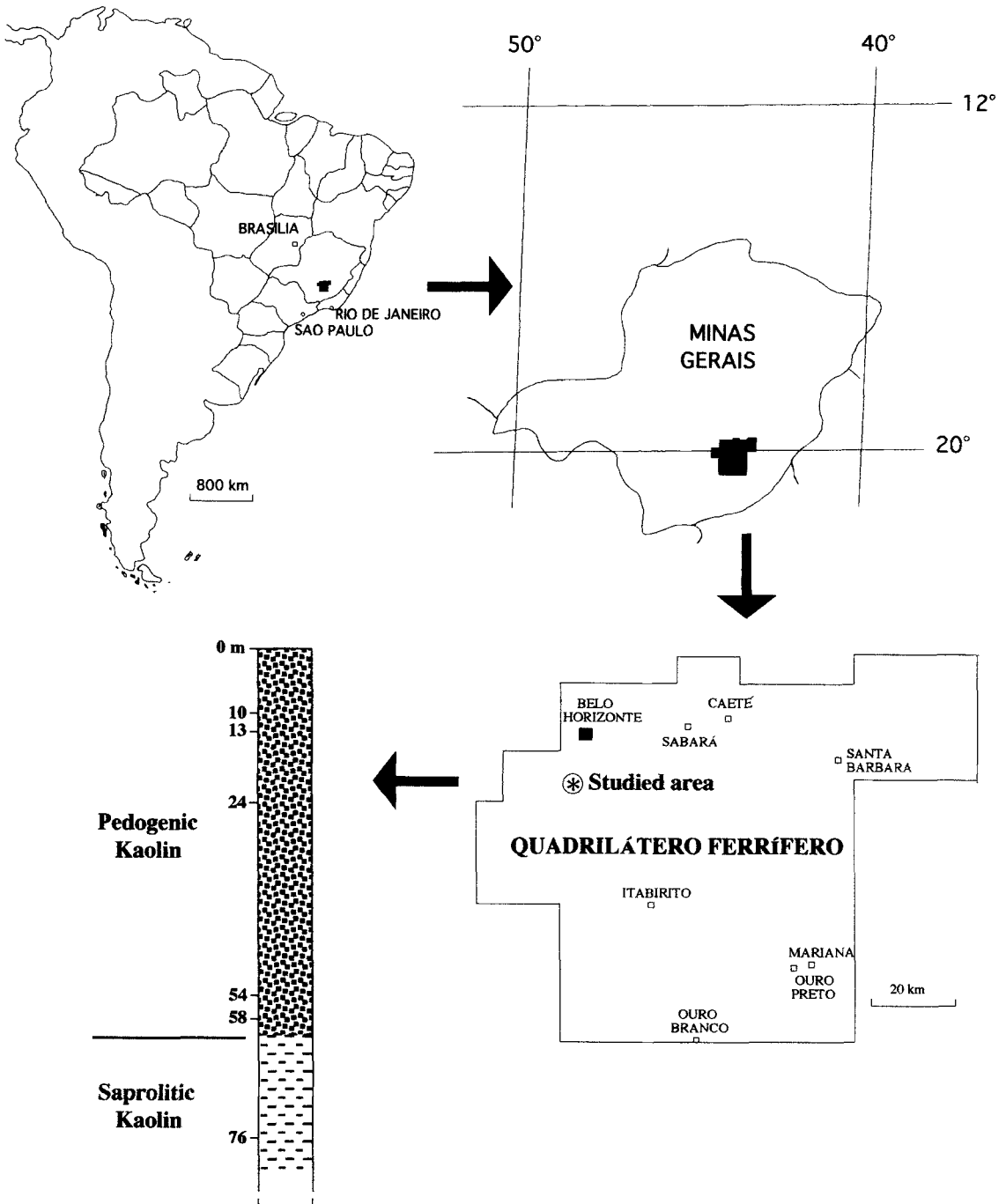
Figure 1. Location of the study area and a schematic core, showing the boundary between the saprolitic and overlying pedogenic kaolin with the sample locations.

tals, micrographs were taken of the dispersed samples. The shape of each crystal was copied using Adobe PhotoShop software. For each sample, >100 crystals were obtained and the area- and shape-distribution functions were determined using NIH Image software, version 6.0. To estimate the shape, we considered the axial ratio (length/width) of the ellipse circumscribed around each particle and that is denominated in this paper as the shape ratio (Sr). An arbitrary value of the length/width ratio of 2.0 was used to calculate the relative proportion of elongated and equant particles in each sample. To complement morphological data from
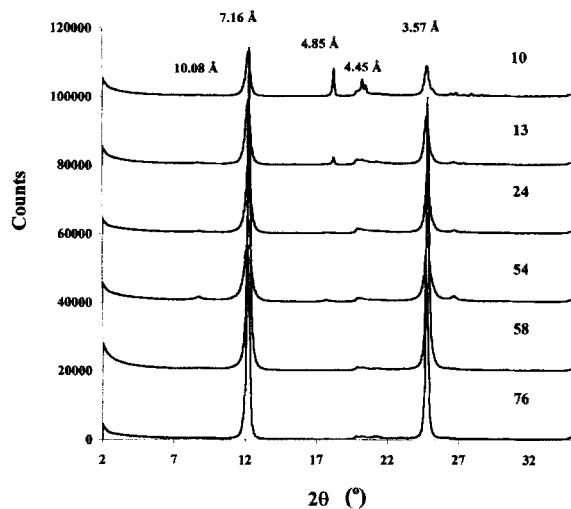
Figure 2. X-ray diffraction patterns (CuKα radiation) of the oriented clay fraction after chemical treatment. From the bottom to the top (samples 76, 58, 54, 24, 13, 10), note that the basal reflections of kaolinite (001, 7.16 Å and 002, 3.57 Å) become less sharp and less intense owing to increasing defects and decreasing crystal size.
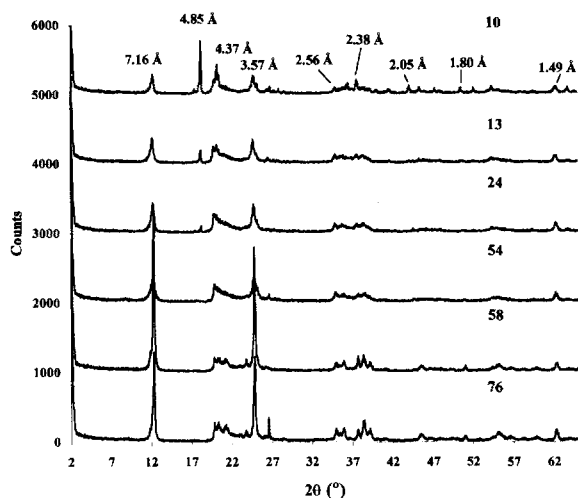
Figure 3. X-ray diffraction patterns (CuKα radiation) of the randomly oriented clay fraction, after chemical treatment to remove iron oxides, showing the mineral distribution in the profile. From the bottom to the top (samples 76, 58, 54, 24, 13, 10), note the decreasing defects of kaolinite with depth marked by the improved resolution of reflections in the range 18–30 and 35–40 °2θ.

TEM, the surface area of the <2-μm size fraction was measured using the N_2-BET method (Aylmore et al., 1970) on a Gemini 2375 V5.00 instrument.

To determine the elemental chemical composition of individual crystals for each dispersed sample, data from EDS for >100 single crystals were collected at 100 s, using a spot size of ~10 nm. A tilt angle of 20° towards the detector was used for all analyses. After background elimination, intensities were converted to analyses using k factors derived from the spectra of standard minerals (Jepson and Rowse, 1975; Lorimer, 1987).

The samples (clay fraction, <2 μm), after chemical treatment, were examined also by EPR to investigate the nature and content of iron in the kaolinite. These data were compared to the morphological and XRD results (Hinckley and HB indexes). X-band EPR spectra were obtained using and ESP 300E (Brucker) spectrometer with an ER41025T cavity. The magnetic field was calibrated using a ¹H-NMR (nuclear magnetic resonance) gaussmeter probe placed at the pole face of the magnet. The microwave modulation was 0.2 mW and spectra were obtained at 120 K from 50-mg samples.

RESULTS AND DISCUSSION

XRD and DTA measurements

The XRD patterns of the unfractionated samples show the dominant presence of kaolinite with minor amounts of gibbsite, quartz, goethite, hematite, and anatase. The iron oxides and gibbsite are concentrated in the upper part of the profile and the former was elim-

inated by the chemical extractions. The XRD patterns of the oriented clay fraction also show minor illite with a variable distribution throughout the profile (Figure 2).

Variations in the FWHM of basal reflections of kaolinite for samples from the bottom (76 and 58 m) and higher are presented in Figure 2. For samples 76 and 58, the range of FWHM values of 0.21–0.26 °2θ corresponds to crystal thicknesses of 353–319 Å. For samples 54, 24, 13, and 10, the range of FWHM values of 0.36–0.44 °2θ corresponds to crystal thickness values of 215–171 Å, which is comparable in size to microcrystalline soil kaolinite described by Singh and Gilkes (1992a).

The Hinckley index (Hinckley, 1963), calculated from the random powder samples of the clay fraction (Figure 3) also showed systematic variations. For samples 76 and 58, the high index values of 0.90 and 0.75 are characteristic of low- to medium-defect densities, respectively. This interpretation is supported by the presence of two sets of triplet peaks in the 35–40 °2θ range which is a characteristic of low-defect kaolinite (Brindley, 1980, p. 146). For other samples, the absence of discrete (1$\bar{1}$0) with d = 4.36 Å and (11$\bar{1}$) with d = 4.18 Å reflections, and the change of the triplet peaks to doublet peaks, characterizes the higher defect density of the kaolinite (Figure 3). As it is not possible to determine the Hinckley index for these high-defect kaolinites, the Hughes and Brown (HB) index (Hughes and Brown, 1979) was calculated. The values of this index ranged from 3.0 to 5.0 (4.0 for sample 58, 5.0 for sample 54, 3.9 for sample 24, 3.2
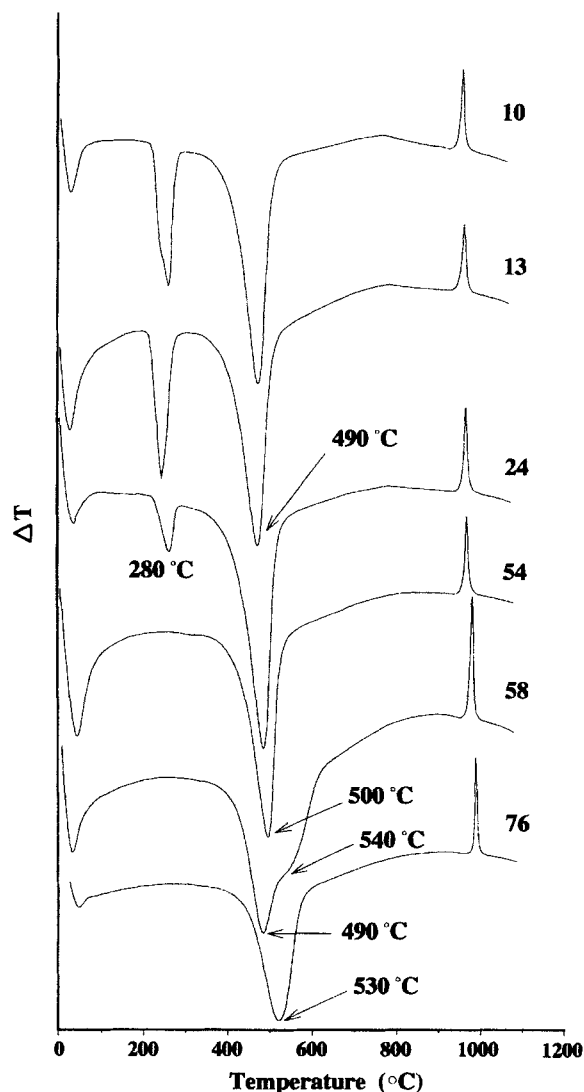
Figure 4. Differential thermal analysis curves for the six samples. Note the variation of the kaolinite endotherm dehydroxylation temperature between sample 76 (530°C) and the other samples (~490°C) and the double peak (540 and 490°C), for sample 58, indicating the presence of two discrete kaolinite phase.

for sample 13, and 3.0 for sample 10) and are typical of soil kaolinites. For sample 76, a value of HB index of 26 is comparable to values reported for reference kaolinites (Hughes and Brown, 1979).

The XRD results are consistent with the DTA analyses (Figure 4) that show a peak temperature of kaolinite dehydroxylation of 530°C for sample 76, indicating a low-defect kaolinite (Grim, 1968). From samples higher in the deposit, dehydroxylation temperatures are ~490°C which is indicative of a high-defect concentration and/or small crystal size. For sample 58, 490 and 540°C peaks occur, indicating the presence of both forms of kaolinite.

ATEM and image analysis

Typical morphology and size of kaolinite crystals are shown in Figures 5 and 6, which clearly demonstrate a systematic trend in crystal morphology with depth in the deposit. At the bottom (sample 76), the crystals are 1–0.5 μm, they occur as hexagonal plates, and have a narrow range in crystal size. These hexagonal crystals are also present in sample 58 together with much smaller crystals (0.1–0.05 μm). The small crystals become the dominant form above 58 m. In samples 13 and 10, irregular plates and laths are present together with hexagonal plates. These qualitative observations are confirmed by the results of quantitative image analysis (Figures 7 and 8) as presented in frequency histograms for the basal area and shape ratio.

The basal-area histograms (Figure 7) are approximately log normal for all samples. The basal-area histogram for sample 76 is roughly symmetric or negatively skewed with a range of values between 0.0476–0.8865 μm² and a mean of 0.2576 μm² (standard deviation = σ = 0.1567). For samples from 58 m and above, the histograms are positively skewed towards larger values, but they narrow progressively upwards by becoming much less skewed. The asymmetry is related to the presence of large particles with a basal area of >0.05 μm². In contrast to sample 76, most particles have basal-area values of <0.05 μm². The mean area decreases: 0.0396 μm² (σ = 0.1567) for sample 58, 0.0481 μm² (σ = 0.0584) for sample 54,

→

Figure 5. Electron micrographs showing the morphology of kaolinite crystals in the six samples studied. A = 76, B = 58, C = 54, D = 24, E = 13, and F = 10. Note the hexagonal plates (~1 μm) in sample 76; the smaller (~0.1 μm) hexagonal crystals in samples 58, 54, 24; the mixture of larger and smaller crystals in sample 58; and the presence of lath-shaped crystals in the shallower samples (13, 10). The scale represented in A (sample 76) is the same for all the other micrographs.

Figure 6. Morphology and size of the crystals in the six samples studied from TEM micrographs, crystal images were extracted using an image processing system from TEM photographs. A = 76, B = 58, C = 54, D = 24, E = 13, and F = 10. The grouping of large and small particles in B, C, and D is to demonstrate the presence of an almost bimodal population of larger and smaller particles. The scale represented in A (sample 76) is the same for all the other micrographs.
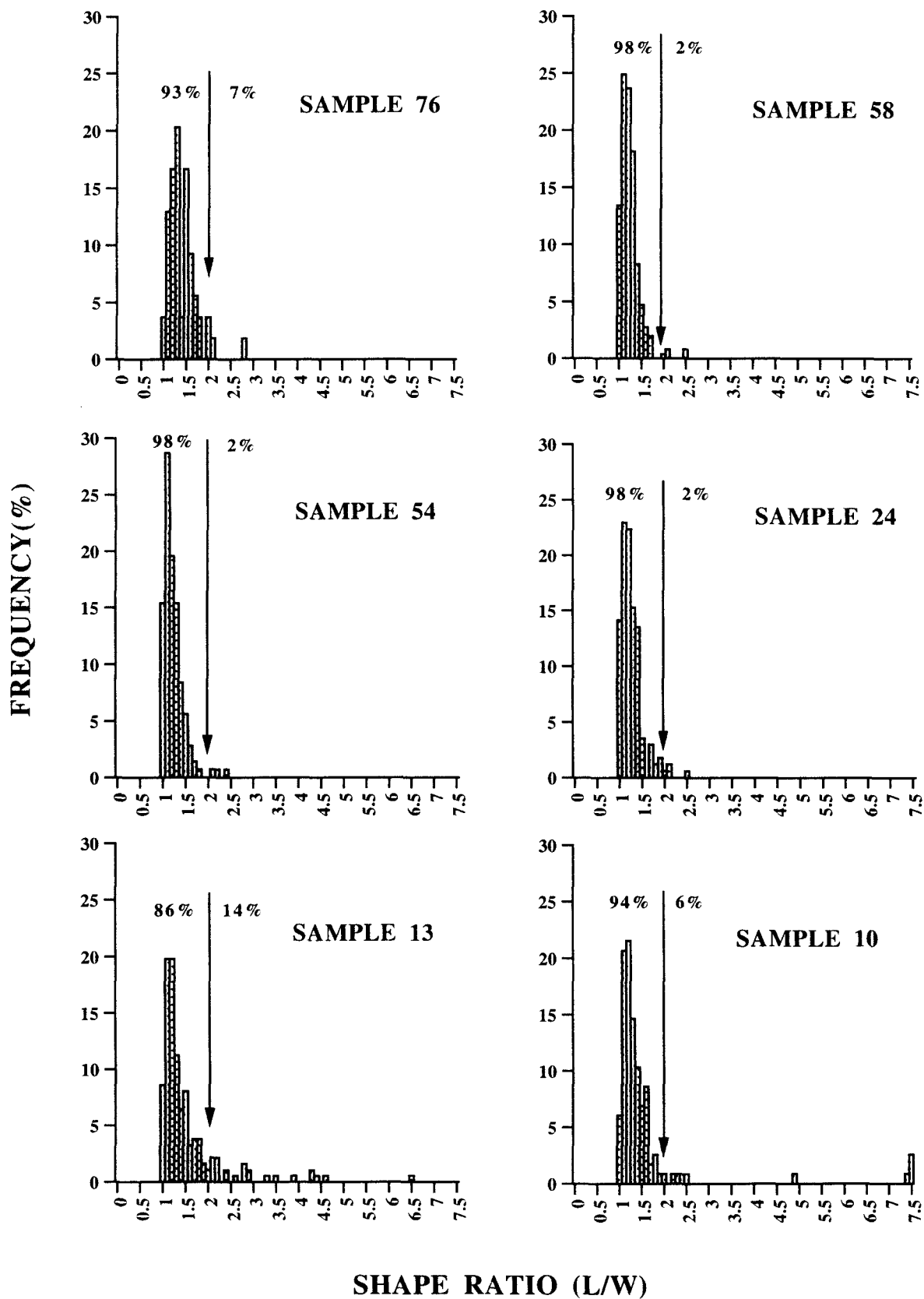
Figure 7. Histograms of particle basal areas. Note the largest particles in sample 76, the asymmetry of the histograms for samples 58–24, indicating mixing of two populations of kaolinites, and the highest concentration of small particles in samples 13 and 10.

Log Basal Area (μm^2)

FREQUENCY(%)

SHAPE RATIO (L/W)
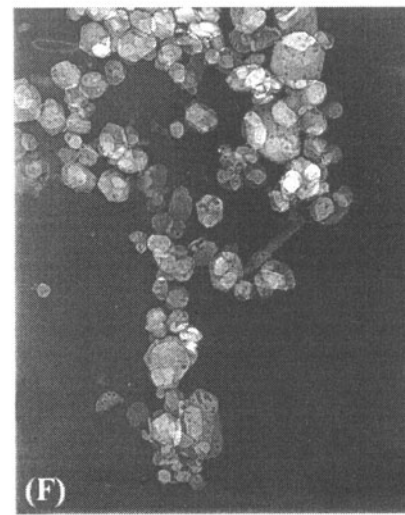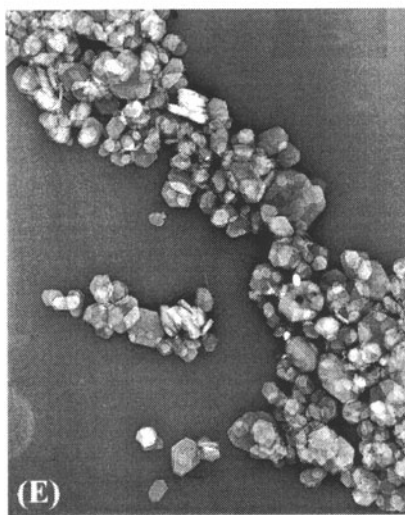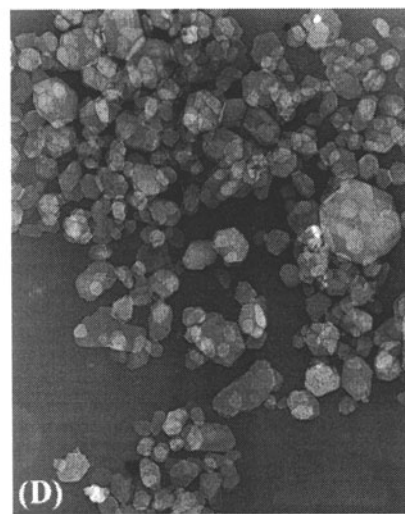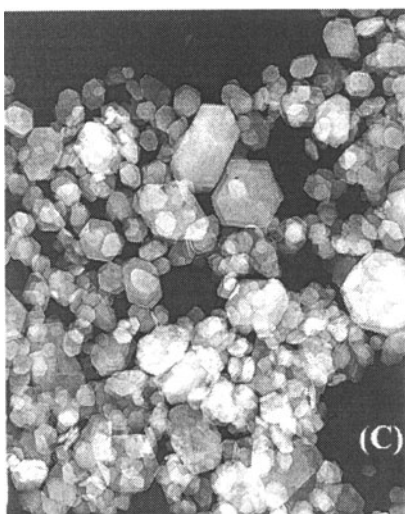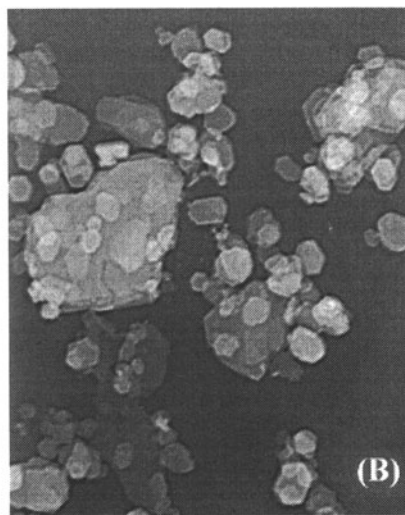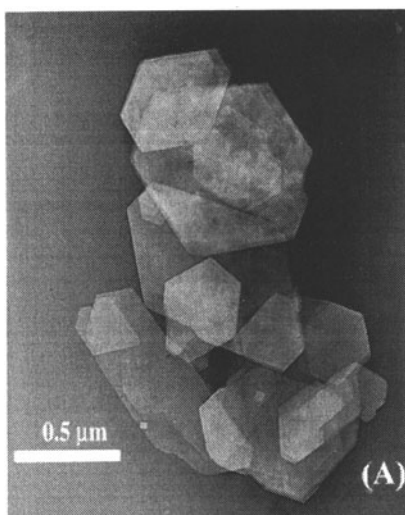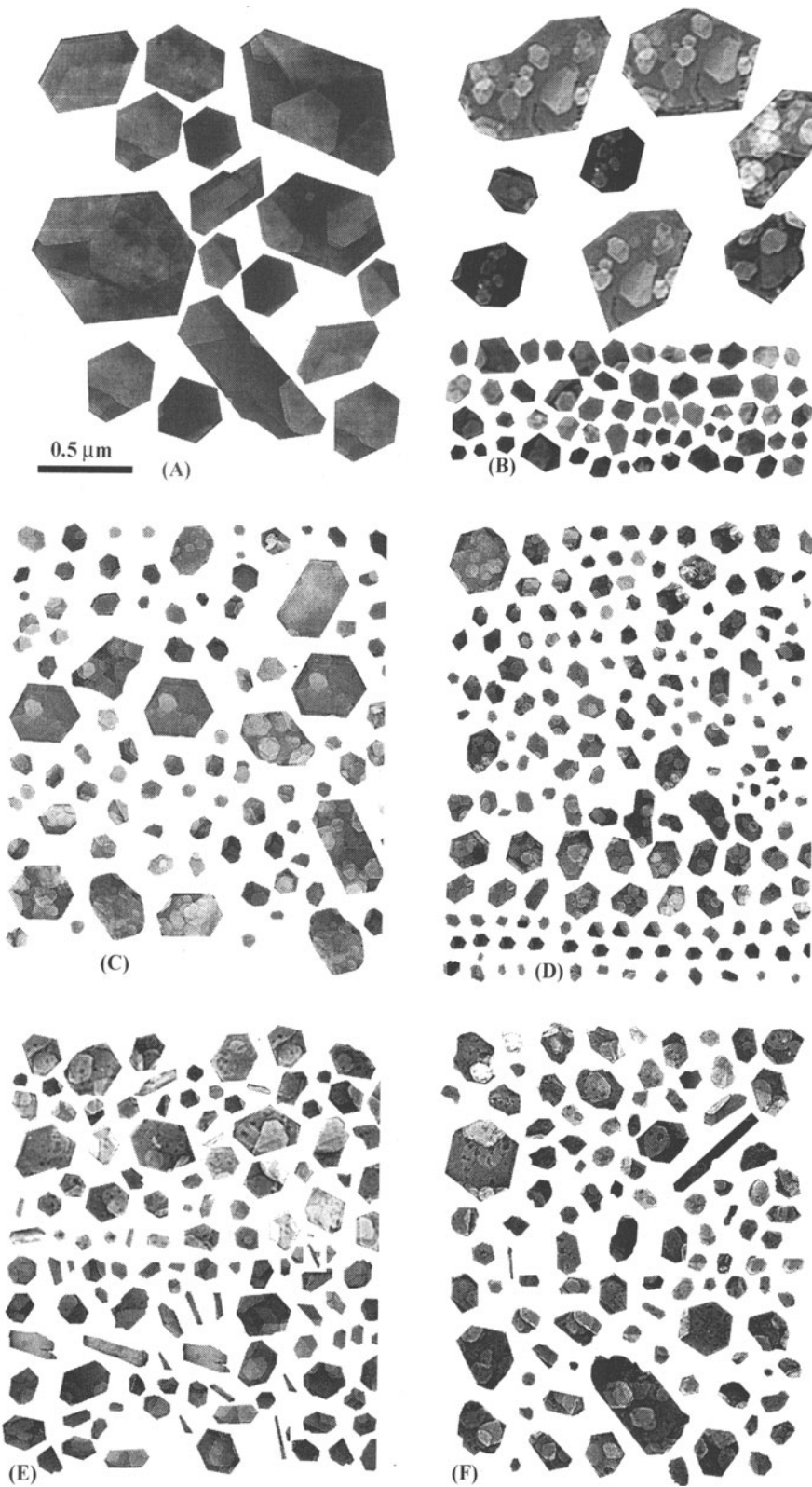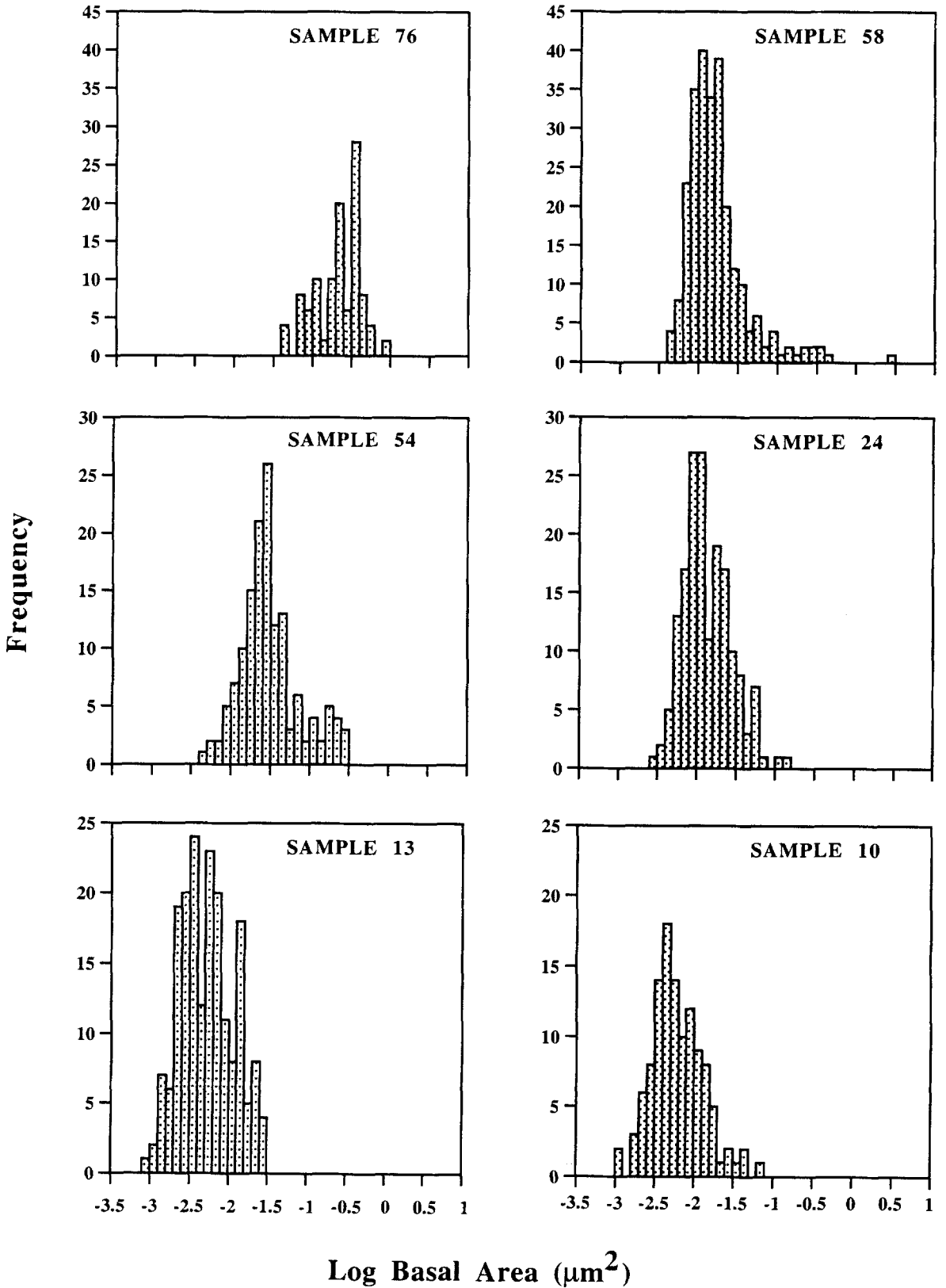
0.0178 μm^2 ($\sigma = 0.0166$) for sample 24, 0.0072 μm^2 ($\sigma = 0.0061$) for sample 13, and 0.0087 μm^2 ($\sigma = 0.0091$) for sample 10, indicating that the number of large particles decreases. The wide variation of crystal size so evident in samples 58, 54, and 24, because some larger crystals are present, still persists in the upper samples as confirmed by the high standard deviation. On the other hand, for sample 76, the standard deviation is ~50% of the mean, which indicates a population of particles with a more uniform area.

The shape-ratio (Sr = L/W, length/width) histograms (Figure 8) are asymmetric because of the presence of elongated particles. The Sr values shift to larger values (Figure 8). To calculate the proportion of lath-shaped and equant (hexagonal or sub-hexagonal) particles, an arbitrary value of Sr = 2.0 was taken as the limit between the two shapes; Sr > 2.0 identifies a lath and Sr < 2.0 identifies an equant crystal. The proportion of lath particles is higher in the samples from the top of the profile, samples 13 and 10, than in samples 24, 54, and 58 (Figure 8). Whereas hexagonal and sub-hexagonal plates are the most common morphological feature of kaolinite crystals (Dixon, 1989), laths are also of widespread occurrence. Both are typical morphologies of pseudomorphous kaolinite occurring in weathering profiles developed by *in situ* evolution. Laths are described by Singh and Gilkes (1992b) as a common morphological feature of kaolinite pseudomorphs after mica. These authors describe bundles of laths originating from a parallel fracturing of a larger plate at regular intervals. These parallel kaolinite laths may be an early stage of formation of halloysite tubes by rolling or folding (Brindley and Comer, 1956; Singh and Gilkes, 1992b). In the present work, we did not observe this last stage either because it requires an appropriate environment or because the laths are unrolled tubes. The quite high frequency (7%) of elongated particles in sample 76 appears to be a typical morphological feature of kaolinitic pseudomorphs after mica in the saprolite. Similarly, the high frequency of elongated particles in the upper samples (samples 13 and 10) compared to the underlying samples (24, 54, and 58) is evidence of a discontinuity in the profile and indicates that the upper samples are a mixture of saprolitic kaolinite crystals and soil kaolinite crystals.

Observations of the extent of uniform lattice fringes of kaolinite aggregates sectioned perpendicular to the basal plane show differences in crystal thicknesses between samples from the saprolite (76 m) and other samples, from 58 m and upwards (Figure 9A and 9B). Defects in layer stacking are observed in all samples

and variations in the basal spacing with occasional 10-Å spacing are also present (Figure 9C). These variations are common in natural kaolinite and are described as occasional interlayers of mica or smectite (Dixon, 1989). Ma and Eggleton (1999) indicated that kaolinite crystals containing 10-Å layers are found in kaolinites of diverse origins and that defects, such as layer dislocation, lateral layer terminations, and cross fringes (Figure 9C and 9D), are common defects within both primary and secondary kaolinite particles. However, in the present work, deformations of the layers (Figure 9D) were observed only in the samples from 58 m and upwards. According to Ma and Eggleton (1999), this kind of defect is particularly common in transported kaolinites, which is consistent with the allochtonous origin of the samples from 58 m and upwards.

Elemental compositions obtained by EDS indicated the presence of only Al and Si in the kaolinite crystals. Despite the presence of minor amounts of discrete illite and interlayers of illite in kaolinite (Figure 9C), the K content was always below the limit of detection, as were Fe and Ti contents. This lack of detection of K may also be partly related to K diffusion from the analyzed region owing to beam damage. Robertson and Eggleton (1991) reported that the replacement of K by H_2O in the transformation of dioctahedral phyllosilicates may render mica less stable. In addition, Ma and Eggleton (1999) reported that beam damage may be concentrated at structural defects or local heterogeneities in composition or structure. Lens-shape zones within the mica lattice were reported by Peacor (1992) as being caused by K diffusion. We have found the same feature within kaolinite, which might also be related to K diffusion from mica inclusions caused by the electron beam.

Figure 10 shows frequency histograms for the Si:Al atom ratio for single crystals in the six samples. The average Si:Al ratio ranges from 0.96 to 1.01 which is close to the theoretical ratio of 1.00 in kaolinite. Statistical analyses of these data indicate that the Si:Al ratio was not significantly different among samples and was not significantly different from 1.00, the ideal value. Much of the variation in Si:Al ratio in Figure 10 may be related to random counting errors and thus not reflect actual differences in composition. Variations in the Si:Al atom ratio are commonly associated with isomorphous replacements of Al by Fe (Jepson and Rowse, 1975) and may be reflected in trends in crystal morphology. However, this was not the case here because no Fe was detected by EDS in the kaolinite crystals (*i.e.*, <0.2%). As discussed below, EPR

←

Figure 8. Histograms of shape ratio (Sr = L/W, length/width). L/W ratio of 2.0 was taken as the boundary between elongated (Sr > 2.0) and equant (Sr < 2.0) particles.
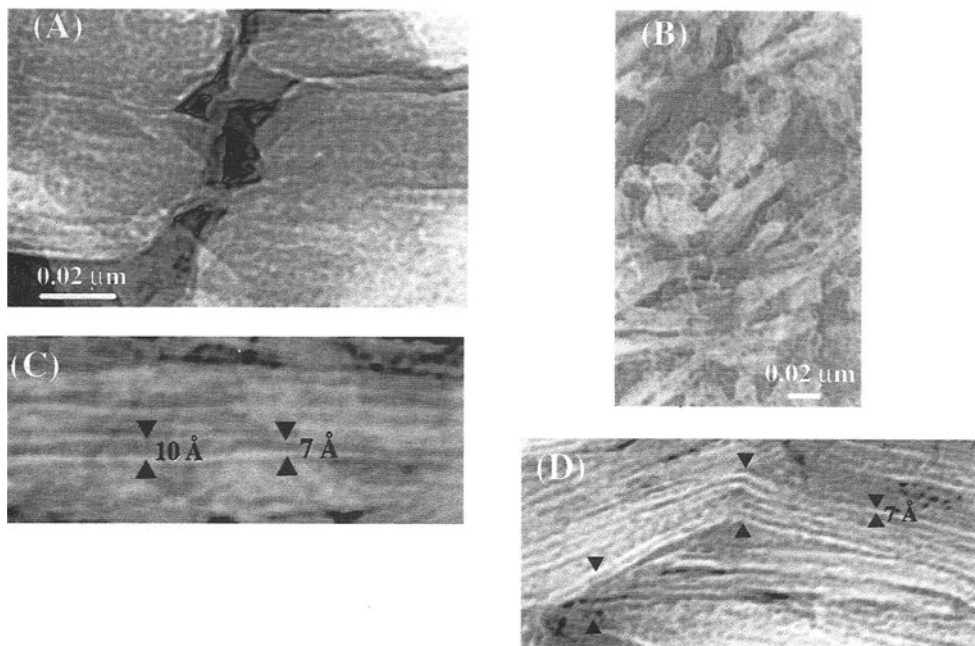
Figure 9. Transmission electron micrographs of microtome sections across the stacks of basally oriented kaolinite particles. A) and B) Low-magnification image showing a side view of plates of kaolinite; note the difference in crystal thickness between sample 76 (A), ~0.03–0.05 μm, and sample 54 (B), ~0.01–0.02 μm. C) and D) are representative images of sample 54 showing the basal lattice fringes with abundant defects marked by arrows. C) Basal spacing of 10–7 Å. D) Lateral layer termination and deformation or bending of several layers.

data indicate that all samples contain minor amounts of iron. Appreciable variations in the composition of individual crystals of kaolinite from soils from southwestern Australia and Georgia kaolin were also described by Singh and Gilkes (1995). Variability in the silica and alumina composition may be useful to discriminate between separate types of kaolinite; Reynolds (1991) found discrete types of kaolinite from different sources based on silica and alumina contents and Hinckley index values. These variations in composition may be related to petrogenic parameters that may have existed at the time of crystallization. However, in this present work, the near constant value of Si:Al of ~1.00 and the similar range of variation in composition for each sample of the clayey sequence studied does not suggest contributions from quite different kaolinitic parent materials.

Chemical composition of the clay fraction

The chemical composition of the clay fraction, determined by XRF after chemical extraction and Ca^{2+} saturation, is presented in Table 1. The Si:Al atom ratios of 1.01, 1.02, 1.00, and 1.02 for samples 76, 58, 54, and 24, respectively, are not significantly different from those obtained from EDS (Figure 10) and from the theoretical ratio of 1:00 for kaolinite. However, Si: Al atom ratios of 1.75 and 1.14, for samples 10 and 13, respectively, reflect the presence of gibbsite as shown in the XRD patterns (Figure 3). Gibbsite in the

clay fraction is ~29 and ~8% for samples 10 and 13, respectively. The TiO_2 content indicates the boundary between the saprolite (sample 76) and samples from 58 m and above. The latter samples with higher TiO_2 contents indicate their residual character.

The appreciable K_2O content in samples 54 and 24 reflect the presence of illite, as indicated also in the XRD patterns. This variable illite distribution in the column is consistent with the allochtonous origin of samples from 58 m and upwards and the variable contribution of illitic sediment.

CEC values are low as is consistent with kaolinitic clay and these values also indicate differences in the nature of the samples. At the bottom, in the saprolite (sample 76), which is characterized by hexagonal particles, the value of CEC of 1.78 cmol/kg is similar to values for low-defect kaolinite in pallid-zone clay and standard kaolinites (Singh and Gilkes, 1992a). For other samples, values range from 3.21 to 4.27 cmol/kg, which are typical of soil kaolinite of pedogenic origin (Singh and Gilkes, 1992a). The presence of small amounts of illite may be responsible for the higher value of 6.42 cmol/kg obtained for sample 54. This value is based on a K_2O content of 6% in soil illite, which represents ~12% illite in this clay. Soil illite has a CEC of ~30 cmol/kg, and therefore 12% illite in the clay soil contributes to ~3.6 cmol/kg of CEC to the clay fraction (Norrish and Pickering, 1983).
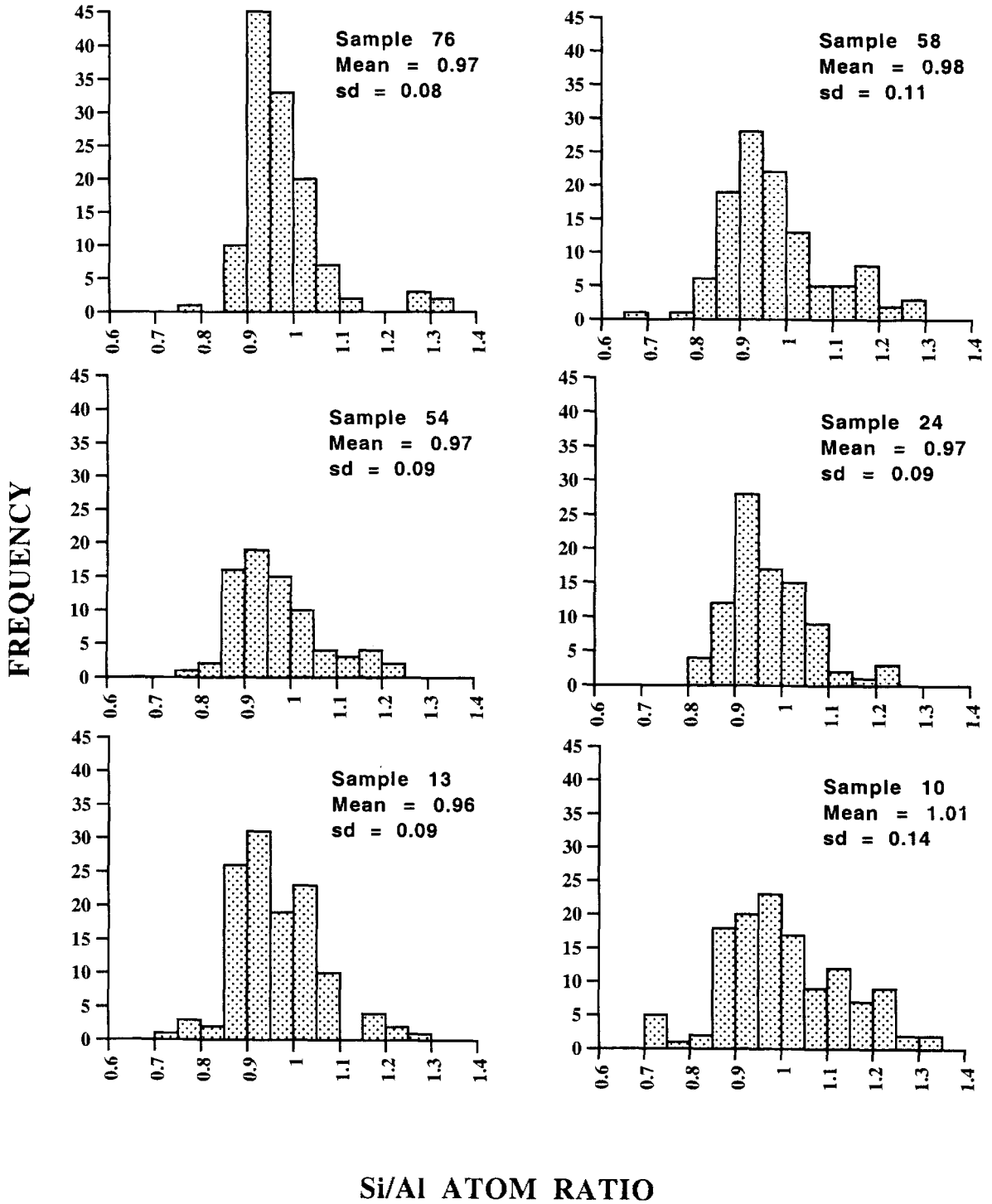
Si/Al ATOM RATIO

Figure 10.   Histograms of atom ratio Si/Al for individual kaolinite crystals plotted against analysis number; sd = standard deviation.

Table 1. Chemical composition (%) and CEC (cmol/kg) of the clay fraction after chemical extractions and Ca^{2+} saturation.

Analysis	Samples					
	10	13	24	54	58	76
SiO_2	30.40	40.00	43.20	43.80	44.00	45.20
Al_2O_3	45.30	38.70	37.50	37.30	38.50	38.90
Fe_2O_3	0.97	1.82	0.85	0.80	0.58	0.39
CaO	0.07	0.12	0.12	0.18	0.09	0.05
MgO	0.03	0.05	0.08	0.13	0.04	0.03
Na_2O	0.04	0.06	0.08	0.10	0.06	<0.01
K_2O	0.05	0.21	0.34	0.70	0.18	0.03
TiO_2	1.96	1.93	2.25	1.64	1.11	0.50
H_2O (105°C)	0.91	1.15	1.01	1.71	1.06	0.59
LOI	21.20	17.20	15.60	15.30	15.50	15.00
CEC	2.49	4.27	4.26	6.42	3.21	1.78

Figure 11. Diagram showing the values of N_2-BET surface area plotted against the values of calculated surface area based on crystal size using Scherrer method.

Surface area

The values of N_2-BET surface area and the calculated surface area based on crystal size as derived from the Scherrer method are represented in Figure 11. Thickness data obtained from the Scherrer method are consistent with observations from microtome sections in the TEM (Figure 9A and 9B). There is good agreement also with values of surface area obtained by BET and Scherrer methods and the plotted data lie close to the line of unit slope. The calculated surface areas, based on the Scherrer equation are higher in value because some particles are compound, *i.e.*, twin-like (Figure 9A and 9B). Thus, the entire surface of the sub-crystals was not accessible for N_2 adsorption. Sample 76 has a surface area from BET of ~10 m^2/g and a calculated area of ~20 m^2/g, which is consistent with its large crystal size and presence of many compound crystals. These values are comparable with those for other standard kaolinites (Dixon, 1989). The value for sample 58 is intermediate between the value for sample 76 and the higher values for samples dominated by pedogenic kaolinite (samples 54, 24, 13, and 10). Soil kaolinites commonly have surface areas of ~35 m^2/g (Singh and Gilkes, 1992a). The anomalous value of sample 10 may be related to the high content of gibbsite with crystal-size values greater (~480 Å) than the kaolinite crystals present in the soil samples (~200 Å), as indicated from the Scherrer equation.

Electron paramagnetic resonance spectroscopy (EPR)

The first-derivative EPR spectra is characterized by the g value, *i.e.*, the spectroscopic splitting factor (Clozel *et al.*, 1994). The g value is an informative parameter, because unpaired electrons in different environments have slightly different g factors, resulting in the appearance of characteristic signals for different centers at different magnetic field strengths. The first-derivative EPR spectra of kaolinite usually consist of two regions, low-field resonances with g = 3.5–4.9,
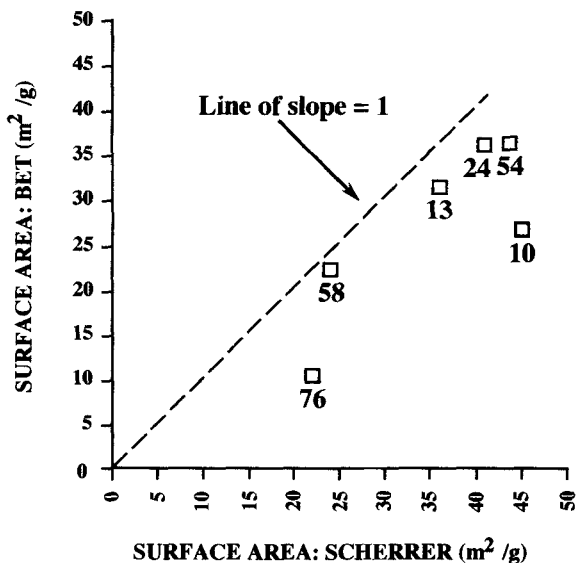
which are associated with Fe^{3+} substituting for Al^{3+}, and high-field resonances with g = 2.0, which are associated with 'A' type radiation-induced defects (RID) (Clozel *et al.*, 1994). In some kaolins, particularly soil kaolins with appreciable iron contents, a very broad resonance extending from g ≈ 3.5 to g ≈ 1.5 (described also as a broad g ≈ 2 peak) occurs. The low-field resonances have been interpreted as the sum of two spectra, $Fe_{(I)}$ and $Fe_{(II)}$. The $Fe_{(I)}$ spectrum (g = 4.3) is associated with stacking disorder and is usually well developed in high-defect and highly iron-substituted kaolinite from soils (Mestdagh *et al.*, 1980). The $Fe_{(I)}$ signal in high-defect kaolinites has recently been associated with dickite C layers (Balan *et al.*, 1999). The $Fe_{(II)}$ spectrum (g = 3.5, 3.7, 4.9, and 9.2) is a consequence of Fe^{3+} for Al^{3+} substitution in low-defect kaolinites. The Q-band spectrum of low-defect kaolinite shows additional resolution of the $Fe_{(II)}$ spectrum for iron. The spectrum is resolved into discrete bands for the two unique octahedral positions in the triclinic unit cell (Gaite *et al.*, 1993).

The first-derivative EPR spectra for the clay fractions of six samples are shown in Figure 12. Samples 54, 24, 13, and 10 show spectra typical of high-defect kaolinite with the g ≈ 4.3 peak from the $Fe_{(I)}$ spectrum dominant in the low-field resonances. Parts of the $Fe_{(II)}$ spectrum are also observable for these samples, g ≈ 9.2 is present but is broad and g ≈ 4.9 is distinguishable as a small shoulder on the main g ≈ 4.3 peak. Sample 76 has a spectrum that is typical of low-defect kaolinite. The peaks at g ≈ 4.9, 3.7, and 3.5 are more prominent; although this resolution is partly related to a reduction in the intensity and width of the g ≈ 4.3
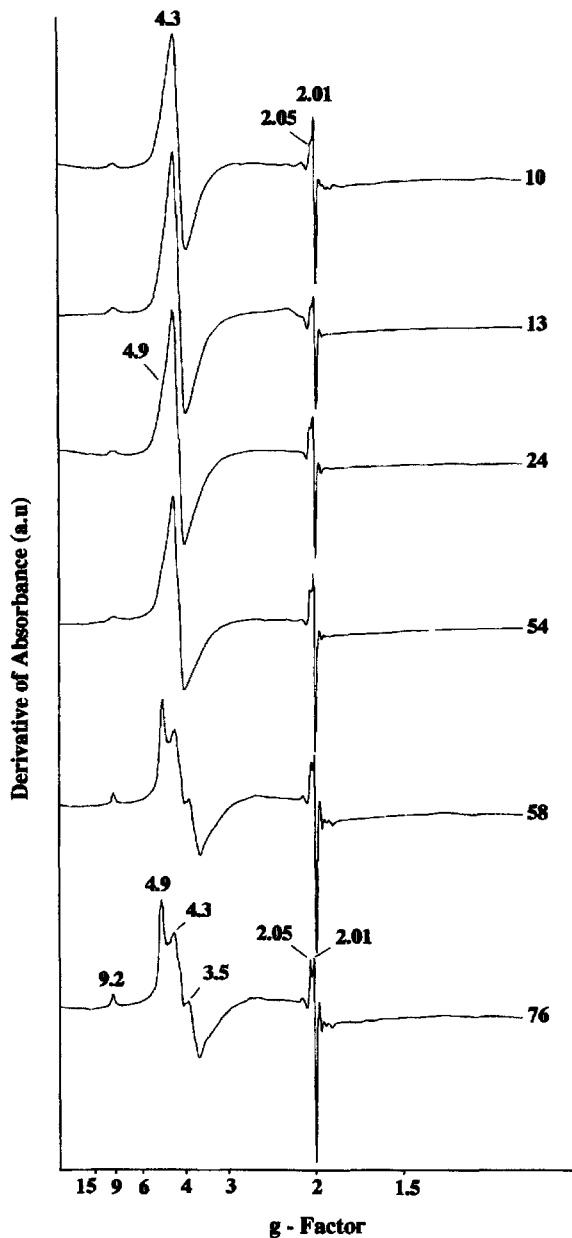
Figure 12. First derivative, X-band EPR spectra of the six samples. Note the typical spectrum of low-defect kaolinite in sample 76 characterized by the prominent peaks at g ≈ 4.9, 3.7, and 3.5 and by the sharp peak at g ≈ 9.2. Note spectra typical of high-defect kaolinite for samples 54, 24, 13, and 10 with the main signal at g ≈ 4.3. Sample 58 shows peaks at g ≈ 4.3 and g ≈ 4.9, 3.7, and 3.5 indicating the presence of a mixture of low- and high-defect kaolinites.

Table 2. Relative concentration of radiation induced defects (RID) and concentration of elements that are potential sources of radiation gamma in whole samples.

Sample	RID Rel. conc.	%Fe$_2$O$_3$	K (ppm)	U (ppm)	Th (ppm)	Pb (ppm)
10	40	6.02	210	4	41	29
13	41	13.69	424	2.80	24	29
24	29	3.29	895	3.9	34	44
54	136	3.83	1083	3.6	28	44
58	34	[1]n.d.	n.d.	n.d.	n.d.	n.d.
76	45	4.10	59	1.1	10	62

[1] n.d.: not determined.

All samples display signals from "A" type RID centers at g ≈ 2.0, which occur in many kaolins and were assigned to a Si-O$^-$ center (Clozel *et al.*, 1994). However, not all kaolins display RID, for example soil kaolins from relatively young red soils in Indonesia and with relatively short exposure to cosmic and mineral radiation sources do not display RID (Hart *et al.*, unpubl. data). Muller and Calas (1989) demonstrated the possibility of determining the relative concentrations of stable defect centers if all other experimental parameters (sample mass, sample packing, placement of sample in cavity, microwave modulation and power, *etc.*) are constant. The relative intensities of the RID in the EPR spectra are given in Table 2 together with analyses of the concentrations of sources of natural γ-radiation in the whole sample; K, U, Th, Pb. The iron-oxide concentration is also given as Muller and Calas (1989) found a relationship suggesting that iron oxy-hydroxides may absorb and retain the γ-emitting elements U and Th in close proximity to the kaolin during the early stages of weathering. The intensity of the RID signals does not change significantly between samples except for sample 54, which has a value approximately four times greater than those of the other samples. There does not appear to be a relationship between RID and any of the other variables identified by Muller and Calas (1989). Perhaps these differences are related to different exposures to cosmic rays or different exposures to regolith isotopes which have now been partly changed.

CONCLUSION

The results obtained from this study clearly show that the deposit consists of a dominant pedogenic kaolin, of colluvial origin, over a saprolitic kaolin with a mixed interface at ~58 m that characterizes the boundary with the saprolite (sample 76). The saprolite is mainly represented by the presence of large (1–0.5 μm) platy particles which are also present to a minor extent in the overlying transported cover (sample at 54 m and upwards). In this cover, variations in shape and size of kaolinite particles define two discrete sources that have contributed to the kaolin deposit.

peak. The g ≈ 9.2 peak is sharper, which is consistent with the low-defect character of this sample (Gaite *et al.*, 1997). Sample 58 is similar but has a stronger g ≈ 4.3 signal which is consistent with the presence of a mixture of smaller particles of high-defect kaolinite and larger particles of low-defect kaolinite.

The chemical, XRD, DTA, BET, ATEM, and EPR data each define a discontinuity between the saprolite (sample 76) and the overlying cover of transported overburden (sample at 58 m and upwards). The clearest definition of the two types of kaolinite was provided by image analysis of TEM images. Despite morphological changes of kaolinite crystals throughout the profile and their distinctly different origins, the elemental composition of single crystals did not change.

Physical parameters of kaolinite crystals were shown to be the best way to differentiate variations in the kaolin deposit and to provide a basis for interpretations of temporal relationships. The heterogenous association in size and morphology of the kaolinite crystals, in the middle and upper part of the profile, may reflect climatic changes after the Miocene, which is the age of formation of the lateritic material in stable soils on the adjoining slopes. During the Pliocene, under arid conditions, erosion became widespread and generated sediments consisting of a mixture of lateritic pedogenic kaolinite and saprolitic kaolinite.

ACKNOWLEDGMENTS

REFERENCES

Angel, B.R., Jones, J.P.E., and Hall, P.L. (1974) Electron spin resonance studies of doped synthetic kaolinite. I. *Clay Minerals*, **10**, 247–255.

Aylmore, L.A.G., Sills, I.D., and Quirk, J.P. (1970) Surface area of homoionic illite and montmorillonite clay minerals as measured by sorption of nitrogen and carbon dioxide. *Clays and Clay Minerals*, **18**, 91–96.

Balan, E., Allard, T., Boizot, B., Morin, G., and Muller, J.-P. (1999) Structural Fe^{3+} in natural kaolinites: New insights from electron paramagnetic resonance spectra fitting at X and Q-band frequences. *Clays and Clay Minerals*, **47**, 605–616.

Barbosa, G.V. (1980) Superfícies de erosão no Quadrilátero Ferrífero, Minas Gerais. *Revista Brasileira de Geociências*, **10**, 89–101.

Blakemore, L.C., Searle, P.L., and Daly, B.K. (1981) A. Methods for chemical analysis of soils. *New Zealand Soil Bureau Scientific Report, 10A,* DSIRO, New Zealand.

Brindley, G.W. (1980) Order-disorder in clay mineral structures. In *Crystal Structures of Clay Minerals and Their Identification*, G.W. Brindley and G. Brown, eds., Mineralogical Society, London, 125–195.

Brindley, G.W. and Comer, J.J. (1956) Structure and morphology of a kaolin clay from Les Eyzies (France). *Clays and Clay Minerals*, **4**, 61–66.

Brindley, G.W., Kao, C-C., Harrison, J.L., Lipsicas, M., and Rayathatha, R. (1986) Relation between structural disorder and other characteristics of kaolinites and dickites. *Clays and Clay Minerals*, **34**, 239–249.

Clozel, B., Allard, T., and Muller, J.P. (1994) Nature and stability of radiation-induced defects in natural kaolinites: New results and a reappraisal of published works. *Clays and Clay Minerals*, **42**, 657–666.

Dixon, J.B. (1989) Kaolinite and serpentine group minerals. In *Minerals in Soils Environments, 2nd edition*. J.B. Dixon and S.B. Weed, eds., Soil Science Society of America, Madison, Wisconsin, 357–403.

Dorr, J.V.N. (1969) *Physiographic, Stratigraphic and Structural Development of the Quadrilátero Ferrífero, Minas Gerais, Brazil.* U.S. Geological Survey Professional Paper 641C, Washington, D.C., 1–58.

Fleisher, R. and Oliveira, V.P. (1969) Bauxitas do Quadrilátero Ferrífero. *Mineração e Metalurgia*, **50**, 25–32.

Gaite, J.-M., Ermakoff, P., and Muller, J.-P. (1993) Characterization and origin of two Fe^{3+} spectra in kaolinite. *Physics and Chemistry of Minerals*, **20**, 242–247.

Gaite, J.-M., Ermakoff, P., Allard, TH., and Muller, J.-P. (1997) Paramagnetic Fe^{3+}: A sensitive probe for disorder kaolinite. *Clays and Clay Minerals*, **45**, 496–505.

Gilkes, R.J., Scholz, G., and Dimmock, G.M. (1973) Lateritic deep weathering of granite. *Journal of Soil Science*, **24**, 523–536.

Grim, R.E. (1968) *Clay Mineralogy, 2nd edition.* McGraw-Hill, New York, 596 pp.

Guggenheim, S., Alietti, A., Drits, V.A., Formoso, M.L.L., Galán, E., Köster, H.M., Paquet, H., Watanabe, T., Bain, D.C., and Hudnall, W.H. (1997) Report of the Association Internationale pour L'étude des Argiles (AIPEA) Nomenclature Committee for 1996. *Clays and Clay Minerals*, **45**, 298–300.

Herbillon, A.J., Mestdagh, M.M., Vielvoye, L., and Derouane, E.G. (1976) Iron in kaolinite with special reference to kaolinite from tropical soils. *Clay Minerals*, **11**, 201–220.

Hinckley, D.N. (1963) Variability in "crystallinity" values among the kaolin deposit of the coastal plain of Georgia and South Carolina. *Clays and Clay Minerals*, **11**, 229—235.

Holmgren, G.G.S. (1967) A rapid citrate-dithionite extractable iron procedure. *Soil Science Society of America Proceedings*, **31**, 210–211.

Hughes, J.C. and Brown, G. (1979) A crystallinity index for soil kaolins and its relation to parent rock, climate and soil maturity. *Journal of Soil Science*, **30**, 557–563.

Jepson, W.B. and Rowse, J.B. (1975) The composition of kaolinite—An electron microscope microprobe study. *Clays and Clay Minerals*, **23**, 310–317.

Jones, J.P.E., Angel, B.R., and Hall, P.L. (1974) Electron spin resonance studies of doped synthetic kaolinite. II. *Clay Minerals*, **10**, 257–270.

Keller, W.D. (1978) Classification of kaolins exemplified by their textures in scan electron micrographs. *Clays and Clay Minerals*, **26**, 1–20.

Klug, H.P. and Alexander, L.E. (1974) *X-ray Diffraction Procedures for Polycrystalline and Amorphous Materials, 2nd edition.* John Wiley and Sons Inc., New York, 966 pp.

Lorimer, G.W. (1987) Quantitative X-ray microanalysis of thin specimens in the transmission electron microscope; A review. *Mineralogical Magazine*, **51**, 49–60.

Ma, C. and Eggleton, R.A. (1999) Surface layer types of kaolinite: A high resolution transmission electron microscope study. *Clays and Clay Minerals*, **47**, 181–191.

McCrea, A.F., Anand, R.R., and Gilkes, R.J. (1990) Mineralogical and physical properties of lateritic pallid zone materials developed from granite and dolerite. *Geoderma*, **47**, 33–57.

McKeague, J.A. and Day, J.H. (1966) Dithionite and oxalate extractable Fe and Al as aids in differentiating various classes of soils. *Canadian Journal of Soil Science*, **46**, 13–22.

Meads, R.E. and Malden, P.J. (1975) Electron spin resonance in natural kaolinites containing Fe^{3+} and other transition metal ions. *Clay Minerals*, **10**, 313–345.

Mestdagh, M.M., Vielvoye, L., and Herbillon, A.J. (1980) Iron in kaolinite: II. The relationship between kaolinite crystallinity and iron content. *Clay Minerals*, **15**, 1–13.

Mulcahy, M.J. (1973) Landforms and soils of south-western Australia. *Journal of the Royal Society of Western Australia*, **56**, 16–22.

Muller, J-P. and Calas, G. (1989) Tracing kaolinites through their defect centers: Kaolinite paragenesis in a laterite (Cameroon). *Economic Geology*, **84**, 694–707.

Muller, J-P., Manceau, A., Calas, G., Allard, T., Ildefonse, P., and Hazemann, J-L. (1995) Crystal chemistry of kaolinite and Fe-Mn oxides: Relations with formation conditions of low temperature systems. *American Journal of Science*, **295**, 1115–1155.

Norrish, K. and Pickering, J.G. (1983) Clay minerals. In *Soils: An Australian Viewpoint*. CSIRO, Melbourne, Academic Press, London, 281–308.

Peacor, D.R. (1992) Analytical electron microscopy: X-ray analysis. In *Minerals and Reactions at the Atomic Scale: Transmission Electron Microscopy, Reviews in Mineralogy, Volume 27*, P.R. Buseck, ed., Mineralogical Society of America, Washington, D.C., 113–140.

Pomerene, J.B. (1964) *Geology and Ore Depositis of the Belo Horizonte, Ibirité and Macacos Quadrangles, Minas Gerais, Brazil*. U.S. Geology Survey Professional Paper 341-D, Washington, D.C., 84 pp.

Reynolds, W.R. (1991) Discrimination of kaolinite varieties in Porters Creek and Wilcox sediments of north-central Mississipi. *Clays and Clay Minerals*, **39**, 316–323.

Robertson, I.D.M. and Eggleton, R.A. (1991) Weathering of granitic muscovite to kaolinite and halloysite and of plagioclase-derived kaolinite to halloysite. *Clays and Clay Minerals*, **36**, 113–126.

Robertson, R.H.S., Brindley, G.W., and Mackenzie, R.C. (1954) Mineralogy of kaolin clays from Pugu, Tanganiyka. *American Mineralogist*, **39**, 118–138.

Robson, A.D. and Gilkes, R.J. (1981) Fertiliser responses (N, P, K, S micronutrients) on lateritic soil in south western Australia—A review. In *Lateritisation Processes*, A.A. Balkema, Rotterdam, The Netherlands, 381–390.

Singh, B. and Gilkes, R.J. (1992a) Properties of soil kaolinites from south-western Australia. *Journal of Soil Science*, **43**, 645–647.

Singh, B. and Gilkes, R.J. (1992b) An electron optical investigation of the alteration of kaolinite to halloysite. *Clays and Clay Minerals*, **40**, 212–229.

Singh, B. and Gilkes, R.J. (1995) Application of analytical transmission electron microscopy to identifying intercrystal variations in the composition of clay minerals. *Analyst*, **120**, 1335–1339.

Souza, J.M. (1983) *Relatório de Pesquisa de Bauxita e Argila no Local Denominado Capão Xavier e Ouro Podre, Nova Lima, MG*. MBR—Minerações Brasileiras Reunidas S.A., Belo Horizonte, 25 pp.

Spurr, A.R. (1969) A low viscosity epoxy resin: Embedding medium for electron microscopy. *Journal of Ultrastructure Research*, **26**, 31–43.

Stone, W.E.E. and Torres-Sanchez, R.-M. (1988) Nuclear magnetic resonance spectroscopy applied to minerals. *Journal of the Chemical Society, Faraday Transactions I*, **84**, 117–132.

Tamm, O. (1922) Eine method zur Geotemmung de anorganischen komponente des glekomplexes in Boden. *Meddelanden fran Statens Skogsförsöksanstalt*, **19**, 387–404.

Varajão, A.F.D.C., Boulange, B., and Melfi, A.J. (1989) The petrologic evolution of the facies in the kaolinite and bauxite deposits of Vargem dos Óculos, Quadrilátero Ferrífero, Minas Gerais, Brazil. *Travaux*, **19**, 137–146.

Varajão, A.F.D.C., Boulange, B., and Melfi, A.J. (1990) Caracterização morfológica, mineralógica e química das fácies estruturais da jazida de caulinita de Vargem dos Óculos, Quadrilátero Ferrífero, MG. *Revista Brasileira de Geociências*, **20**, 75–82.

Varajão, A.F.D.C., Rocha, L.A., Boulange, B., and Moreira, A.P.A. (2000) Colluvial features of clayey deposits of the Moeda Syncline, Quadrilatero Ferrifero, Minas Gerais, Brazil. *Zentralblat Fur Geologie und Palaontologie*, Teil 1, *7/8*, 957–968.

E-mail of corresponding author: angelica@degeo.degeo.ufop.br